ISSN 1070-4280, Russian Journal of Organic Chemistry, 2025, Vol. 61, No. 10, pp. 1942–1958. © Pleiades Publishing, Ltd., 2025.

Synthesis, Characterization (IR, NMR), DFT Calculations, Gamma-Ray Absorption, Antimicrobial Activity, and In Silico Study of Imidazole Derivatives

N. Süleymanoğlu[a,*], Y. Ünver[b], A. Coşkun[c], R. Ustabaş[d], F. Çelik[b], H. İ. Güler[e], and K. I. Bektaş[e]

[a] *Advanced Technologies, Graduate School of Natural and Applied Sciences, Gazi University, Ankara, 06500 Turkey*

[b] *Department of Chemistry, Faculty of Sciences, Karadeniz Technical University, Trabzon, 61080 Turkey*

[c] *Vocational School of Health Services Department, Toros University, Mersin, 33140 Turkey*

[d] *Department of Mathematics and Science Education, Educational Faculty, Ondokuz Mayıs University, Kurupelit, Samsun, 55139 Turkey*

[e] *Department of Molecular Biology and Genetics, Faculty of Sciences, Karadeniz Technical University, Trabzon, 61080 Turkey*

**e-mail: nevinseylan@gmail.com*

Received April 25, 2025; revised May 10, 2025; accepted May 14, 2025

Abstract—New imidazole derivatives **2a**–**2c** were synthesized and characterized by FT-IR and NMR spectroscopic methods. Density functional theory (DFT) method with 6-311++G(*d*,*p*) basis set was used for the theoretical study of compounds **2a**–**2c**. To make it comparable with experimental data, the IR study was carried out in the gaseous state and NMR study was carried out in DMSO as a solvent. The obtained structural and spectral data confirmed the molecular structures of compounds **2a**–**2c**. Gamma ray shielding parameters of compounds **2a–2c** were examined with Monte Carlo-based Geant4/GATE, Phy-X/PSD, and XCOM simulations. The newly synthesized compounds were assessed for their antimicrobial properties against nine pathogenic microorganisms responsible for various diseases. The molecular docking simulations were conducted using the 3D structures of key bacterial proteins with compound **2a** to examine the critical interactions responsible for its antibacterial activity, considering the results obtained for the bacterium *E. faecalis*.

Keywords: imidazole, synthesis, IR, NMR, DFT, gamma-ray, antimicrobial activity, in silico study

DOI: 10.1134/S1070428025601293

INTRODUCTION

Drugs containing heterocyclic cores show high chemotherapeutic properties and make significant contributions to the development of new drugs. There are many heterocyclic compounds in clinical use in the treatment of many diseases. Therefore, drugs containing heterocyclic rings are of great importance. Imidazole, also known as 1,3-diazole, is a five-membered heterocyclic compound containing three carbon and two nitrogen atoms. Imidazole compounds constitute an important area of research in pharmaceutical chemistry due to their ability to treat many harmful and malignant diseases. Imidazole derivatives show many biological activities, such as antifungal [1], antibacterial [2], anti-inflammatory [3], histamine H3 anatognistic [4], antimalarial [5], antioxidant [6], antiparasitic [7], farnesyltransferase and geranylgeranyltransferase-I inhibitory [8], antitumor [9], antiprotozoal [10], and antidiabetic [11]. Various drugs with trisubstituted imidazole ring such as Dimetridazole, Azathioprine, Carnidazole, Mezlocillin, Mizoribine, and Ronidazole are available in the market [12, 13]. Moreover, histidine is the basic nucleus of some natural products such as purine, histamine, and DNA-based structures [14].

Schiff bases are compounds containing a carbon–nitrogen double bond (CH=N) that are obtained via nucleophilic addition of aldehydes or ketones and amines [15]. Schiff bases (imines) have been among the compounds of interest because they are stable and easy to synthesize. The interest in imines can be explained by their use in many biological systems [16], chemical catalysis [17], medicine and pharmacy [18], chemical analysis and new technologies [19, 20]. The importance of coordination compounds in both biological systems and industry is increasing day by day. Schiff bases are among the ligands widely used in coordination chemistry due to their structural and biological properties. Metal complexes of Schiff bases as ligands are extensively studied [21, 22]. The use of metal imine complexes as antitumor agents and herbicides has been widely investigated [23]. They have been reported to have a protective effect on the hematopoietic system [24]. In addition to their antiviral uses, they are also considered antibacterial and antifungal agents and are also used in the treatment of diabetes and AIDS [25–27]. In addition, Schiff bases are used in many areas such as corrosion prevention, cation transport, ion-selective electrode production, and paint industry [28].

With increase in radiation applications in almost every field due to the advancement of technology, radiation protection has become even more important. Direct exposure to ionizing radiation causes many health problems, including genetic damage, organ failure, cancer, and dermatological disorders [29]. Shielding is used to reduce exposure to radiation. Many factors such as attenuation effectiveness against ionizing radiation, thermal, chemical, and mechanical properties, corrosion resistance, flexibility, lightness, toxicity, and cost efficiency affect the selection of materials for radiation protection. In particular, materials with different molecular weights are selected depending on the type of radiation applied. For example, hydrogen-rich materials are suitable for neutron shielding, materials with high atomic number (*Z*) elements are used for gamma rays and X-rays. Since neutrons are uncharged subatomic particles that can only interact with the target atom nuclei, the probability of a particular type of interaction depends on two fundamental factors, namely the energy of neutron and specific properties of the target nucleus [30]. Compounds with high atomic numbers are good gamma shielding materials, while compounds with low atomic numbers are suitable for neutron shielding. Experimental and theoretical methods are used in material studies. In the literature, simulation programs are used in the search for radiation shielding materials, as well as experimental methods, due to their low chance of error and accessibility. The mass absorption coefficients of B_4C- and $NaB_5O_8{\cdot}5H_2O$-doped concretes were calculated using the Fluka Monte Carlo method code and the photon energies were found to be consistent with the literature data [31]. The results of GEANT4 simulation of aluminum, silicon, carbon, phosphorus, sulfur, chromium, manganese, titanium, and iron at different ratios with molybdenum, nickel and copper were compared with those obtained by WinXCOM [32]. Wu et al. [33] examined the photon absorption properties of lead borate compounds with the chemical formula $Pb_3B_{10}O_{16}(OH)_4$ and concluded that they are very effective in protecting against neutron and γ radiation [33]. Abou Hussein et al. [34] added 2 wt % PbO, BaO, or SrO to the lithium bismuth silicate glass composition and compared the experimental and theoretical mass attenuation coefficients using the NaI (Tl) detector and Phy-X/PSD software. Oxide compounds and heavy metals were used as gamma-ray shielding materials. However, especially at low radiation energies, structures containing C, H, N, and O can be used in a wide area because they are lighter than heavy metals. In recent years, antimicrobial research has gained significant importance due to the alarming increase in antibiotic-resistant pathogens and the pressing need for novel therapeutic options. The emergence of resistant Gram-positive and Gram-negative bacterial strains, along with opportunistic fungal infections, poses a major global health threat that current antibiotics often struggle to resolve. Discovering new compounds with strong broad-spectrum antimicrobial properties is crucial in addressing these challenges. Organic synthesis presents a valuable path for developing new antimicrobial agents that can effectively target resistant microorganisms and bridge the gap left by existing treatments. As such, evaluating the antimicrobial efficacy of newly synthesized compounds is a key step in identifying promising candidates for future therapeutic use [35].

For this purpose, in this study, new imidazole compounds, (*E*)-1-(4-butoxyphenyl)-*N*-[3-(1*H*-imidazol-1-yl)propyl]methanimine (**2a**), (*E*)-*N*-[3-(1*H*-imidazol-1-yl)propyl]-1-[4-(pentyloxy)phenyl]methanimine (**2b**), and (*E*)-1-[4-(hexyloxy)phenyl]-*N*-[3-(1*H*-imidazol-1-yl)propyl]methanimine (**2c**), were prepared and characterized by FT-IR and NMR spectroscopic methods. DFT study was performed to examine the details of their molecular structure. The gamma-ray

shielding parameters of compounds **2a**–**2c** were examined using XCOM, GATE, and Phy-X software, and their antimicrobial properties against nine different pathogenic microorganisms were evaluated.

RESULTS AND DISCUSSION

The synthetic pathway for the preparation of compounds **2a**–**2c** is illustrated in Scheme 1. The IR spectra of **2a**–**2c** lacked absorption bands typical of the aldehyde and amine groups of the initial compounds. Proton signal of the N=CH group, which evidences the Schiff base formation, was observed in the ^{1}H NMR spectra as a singlet at δ 8.22, 8.23, and 8.22 ppm for compounds **2a**–**2c**, respectively. As expected, protons belonging to the imidazole and benzene rings were observed in the aromatic region, and protons belonging to alkyl groups were observed in the aliphatic region of the ^{1}H NMR spectra. The CH=N carbon signals appeared at δ_C 161.15 (**2a**), 161.15 (**2b**), and 161.22 ppm (**2c**) in the ^{13}C NMR spectra. Carbon signals of the imidazole and benzene rings and aliphatic groups were observed within the expected ranges. Thus, the IR and NMR spectroscopic data confirmed the structure of **2a**–**2c**.

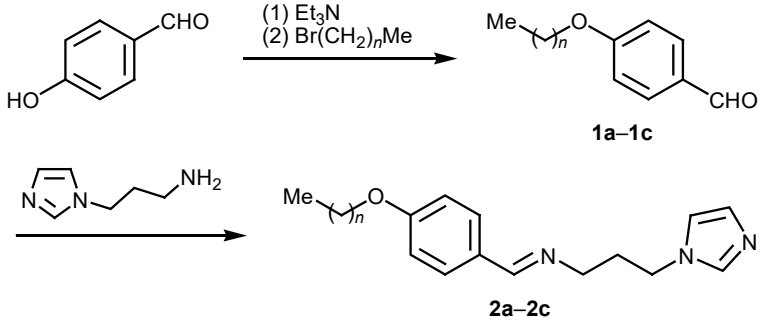
Geometry optimization. Compounds **2a**–**2c** have a benzene ring and an imidazole ring in their structure, and the DFT B3LYP/6-311++G(*d*,*p*) method was used for their geometry optimization. Some of the optimized molecular structure parameters of compounds **2a**–**2c** are presented in Table 1, and the optimized structures are shown in Fig. 1. Compounds **2a**, **2b**, and **2c** differ from each other in the group attached to C^6 of the benzene ring. These groups are butoxy, pentyloxy and hexyloxy, respectively. The inductive effects of these groups on bond lengths, bond angles and torsion angles were investigated.

As seen in Table 1, the bond lengths, bond angles, and torsion angles in molecules **2a**–**2c** are very close to each other. This is the result of the fact that these groups do not have an inductive effect on the structure parameters. The inductive effects of these groups on the dihedral angles between the benzene ring and the imidazole ring in the structure of the three molecules were also examined. The dihedral angles between the benzene and imidazole rings of **2a**, **2b**, and **2c** are 77.92°, 78.53°, and 77.76°, respectively. Butoxy, pentyloxy and hexyloxy groups do not show an inductive effect on the dihedral angles.

Since the bond lengths and bond angles in the optimized structures refer to the gas phase, literature comparison was done with the bond lengths and bond angles determined by X-ray diffraction. The C–O bond lengths in molecules **2a**, **2b**, and **2c** are 1.432/1.359, 1.431/1.360, and 1.431/1.359 Å, respectively. Based on the literature data, these bond lengths are 1.443(2)/1.349(2), 1.4381(14)/1.3706(15), and 1.4447(17)/1.3502(18) Å [36–38], respectively. The C–N and C=N bond lengths in the imidazole ring are 1.381/1.367 and1.314 Å against experimental bond lengths of 1.3769(14)/1.3544(14), 1.388(2)/1.374(2), and 1.3153(16)/1.311(2) Å [39, 40], respectively. The C^{32}O^{11}C^6 bond angle in **2a**, **2b**, and **2c** is 119.3°, 119.2°, and 119.4°, respectively, while the literature bond angle is 118.7(2)° [41]. Thus, the DFT B3LYP/6-311++G(*d*,*p*) method chosen for the optimization is appropriate.

IR and NMR study. The IR and NMR spectral data of compounds **2a**–**2c** were simulated at the DFT B3LYP/6-311++G(*d*,*p*) level, and the results are listed in Tables 2 and 3 together with the experimental data. As seen in Table 2, the bands confirming the molecular structure of **2a**–**2c** were observed at 1643/1642/1642 cm^{-1} for C=N and at 1243/1245/1244 cm^{-1} for C–O–C, respectively. The corresponding calculated

Scheme 1.



n = 3 (**a**), 4 (**b**), 5 (**c**).

Table 1. Some optimized geometric parameters of compounds **2a**–**2c** obtained by the DFT B3LYP/6-311++G(*d*,*p*) method

Bond or angle	**2a**	**2b**	**2c**
Bond lengths, Å			
C^1–C^2	1.395	1.395	1.395
C^2–C^3	1.396	1.396	1.396
C^3–C^4	1.407	1.407	1.407
C^4–C^5	1.381	1.381	1.381
C^5–C^6	1.406	1.406	1.406
C^6–C^1	1.398	1.398	1.397
C^6–O^{11}	1.359	1.360	1.359
O^{11}–C^{32}	1.432	1.431	1.431
C^{32}–C^{33}	1.522	1.520	1.520
C^3–C^{12}	1.470	1.470	1.470
C^{12}–N^{13}	1.272	1.272	1.272
N^{13}–C^{14}	1.454	1.454	1.454
C^{14}–C^{15}	1.534	1.534	1.534
C^{15}–C^{16}	1.533	1.533	1.533
C^{16}–N^{20}	1.460	1.460	1.460
N^{20}–C^{17}	1.381	1.381	1.381
C^{17}–C^{18}	1.372	1.372	1.372
C^{18}–N^{24}	1.375	1.375	1.375
N^{24}–C^{19}	1.314	1.314	1.314
C^{19}–N^{20}	1.367	1.367	1.367
Bond angle, deg			
$C^{32}O^{11}C^6$	119.3	119.2	119.4
$O^{11}C^6C^1$	124.7	124.7	124.7
$O^{11}C^6C^5$	115.7	115.7	115.6
$C^2C^3C^{12}$	119.7	119.8	119.8
$C^4C^3C^{12}$	122.0	122.0	121.9
$C^3C^{12}N^{13}$	122.8	122.8	122.8
$C^{12}N^{13}C^{14}$	121.4	121.5	121.5
$C^{15}C^{16}N^{20}$	113.3	113.3	113.3
$C^{16}N^{20}C^{19}$	126.8	126.7	126.7
$C^{16}N^{20}C^{17}$	126.9	126.9	126.9
Torsion angle, deg			
$C^{32}O^{11}C^6C^1$	1.54	0.08	0.64
$C^{32}O^{11}C^6C^5$	–178.54	–179.91	179.37
$C^2C^3C^{12}N^{13}$	179.99	–179.87	179.87
$C^4C^3C^{12}N^{13}$	0.06	0.08	–0.14
$C^3C^{12}N^{13}C^{14}$	–179.94	179.90	179.95
$C^{12}N^{13}C^{14}C^{15}$	0.89	0.69	0.28
$C^{14}C^{15}C^{16}N^{20}$	179.68	179.56	178.92

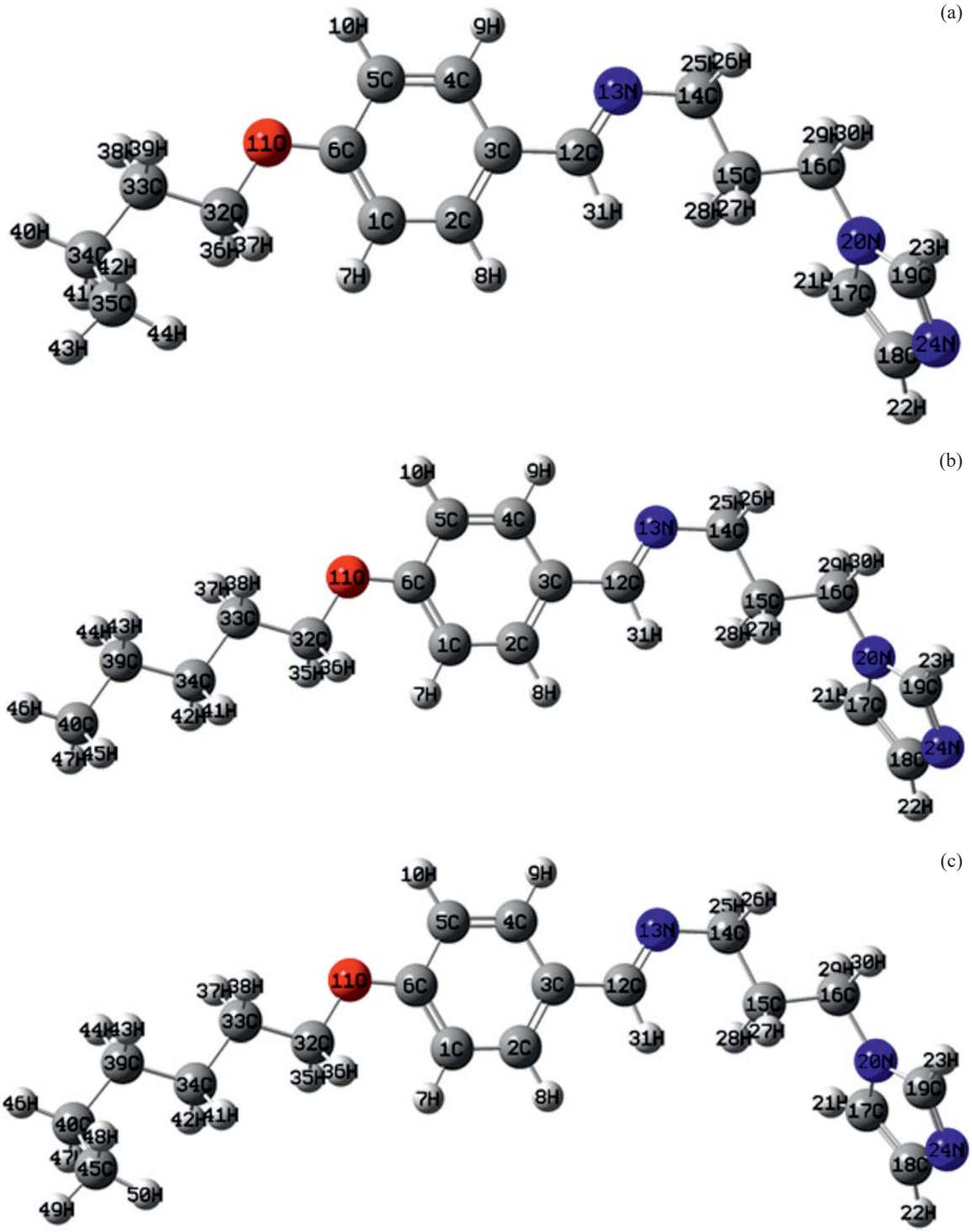


Fig. 1. Molecular structures of compounds (a) **2a**, (b) **2b**, and (c) **2c**, optimized at the DFT B3LYP/6-311++G(*d*,*p*) level of theory.

frequencies are 1642/1642/1641 cm^{-1} for C=N and 1249/1248/1250 cm^{-1} for C–O–C, respectively. Therefore, it can be stated that the selected DFT method is quite suitable for modeling the molecular structure of compounds **2a**–**2c**.

The NMR spectra of **2a**–**2c** were recorded in DMSO-d_6 (see Supplementary Materials). For NMR calculations, the molecular structures were first optimized for DMSO solvent. As can be seen in Table 3, the N=**C**^{12}H signals for compounds **2a**–**2c** were ob-

Table 2. Some experimental and scaled theoretical vibration frequencies (cm^{-1}) of compounds **2a**–**2c**

Assignment	2a		2b		2c	
	experimental	calculated	experimental	calculated	experimental	calculated
ν(C–H_{arom})	2933	3126–3024	2933	3126–3024	2930	3126–3024
ν(C–H)	2933	2961–2869	2933	2961–2865	2930	2961–2866
ν(C=N)	1643	1642	1642	1642	1642	1641
ν(C=C)	1604	1619	1604	1619	1604	1619
ν(C–O–C)	1243	1249	1245	1248	1244	1250

Table 3. Experimental and calculated ^{1}H and ^{13}C NMR chemical shifts (δ, $δ_C$, ppm) of compounds **2a**–**2c**

Nucleus	2a		2b		2c	
	experimental	calculated	experimental	calculated	experimental	calculated
N=**C**H	161.15	164.39	161.15	164.44	161.22	164.71
C_{arom}	114.70, 129.16, 129.99, 161.12	114.37, 140.89, 136.25, 132.10, 124.22, 170.44	114.90, 129.17, 129.98, 161.10	113.97, 140.80, 136.34, 132.36, 124.64, 169.75	114.71, 129.08, 129.98, 161.10	114.29, 140.99, 136.42, 132.44, 124.47, 170.06
C^2, C^4, C^5	119.65, 128.75, 137.72	126.28, 136.54, 144.24	119.66, 128.67, 137.63	126.22, 136.40, 144.44	119.56, 128.75, 161.22	126.36, 137.01, 144.21
N–**C**H_2	32.42, 44.53, 57.62	59.31, 35.57, 51.04	32.42, 44.52, 57.63	59.09, 35.49, 51.03	32.35, 44.52, 57.63	59.63, 35.22, 50.94
O**C**H_2(**C**H_2)$_n$	19.18, 31.13, 67.76	72.50, 35.17, 23.80	22.36, 28.02, 28.63, 68.04	73.40, 34.80, 33.32, 30.00, –	22.55, 25.63, 29.05, 31.47, 68.05,	73.25, 35.26, 28.40, 37.33, 27.60
CH_3	14.13	14.80	14.36	16.67	14.35	14.30
N=C**H**	8.22	8.45	8.23	8.48	8.22	8.48
H_{arom}	7.65–7.69	6.98, 7.56, 8.41, 7.20	7.64–7.69	6.97, 7.55, 8.48, 7.23	7.64–7.69	6.99, 7.59, 8.50, 7.56
4-H, 5-H, 2-H	6.91, 6.98, 7.20	7.39, 7.29, 7.67	6.91, 6.98, 7.20	7.40, 7.28, 7.67	6.91, 6.98, 7.20	7.41, 7.33, 7.67
NC**H**$_2$C**H**$_2$C**H**$_2$N	2.00–2.07, 3.46, 3.97–4.06	4.07, 4.09, 2.09, 2.26, 4.00, 4.06	2.00–2.07, 3.46, 3.97–4.06	4.10, 4.08, 2.09, 2.26, 4.01, 4.03	2.00–2.07, 3.46, 3.97–4.06	4.08, 4.08, 2.13, 2.27, 3.98, 4.07
OC**H**$_2$(C**H**$_2$)$_n$	1.38–1.47, 1.66–1.73, 3.97–4.06	3.83, 4.13, 2.14, 1.87, 1.74, 1.56	1.28–1.42, 1.67–1.73, 3.97–4.06	3.91, 3.91, 1.85, 1.85, 1.29, 1.29, 1.51, 1.51,	1.28–1.30, 1.36–1.41, 1.66–1.73, 3.96–4.04	3.94, 3.91, 1.83, 1.80, 1.59, 1.07, 1.37, 1.72, 1.62, 1.42
C**H**$_3$	0.92	0.88, 1.18, 1.11	0.89	0.97, 1.15, 0.97	0.86	0.73, 1.11, 1.21

served at δ_C 161.15/161.15/161.22 ppm against the calculated chemical shifts δ_C 164.39/164.39/164.71 ppm, respectively. The **C**H_3 signals of **2a**–**2c** were observed at δ_C 14.13/14.36/14.35 ppm, and the calculated values are δ_C 14.80/16.67/14.30 ppm, respectively. The N=C**H**[31] proton signal was located at δ 8.22/8.23/8.22 ppm in the ^{1}H NMR spectra (calculated values δ 8.45/8.45/8.45 ppm, respectively).

Gamma-ray absorption. The molecular weights and densities of the synthesized compounds are given in Table 4. The mass absorption coefficients of **2a**–**2c** were calculated using three theoretical programs and are given in Table 5.

The linear absorption coefficients (LAC) were calculated by substituting the mass absorption coefficients (MAC) according to Eq. (2) (see Experimental). The half-value thickness (HVL) and mean free path (MFP) values were calculated by Eqs. (3) and (4). The graphs obtained for compounds **2a**, **2b**, and **2c** are presented in Figs. 2–4, respectively.

Table 5 gives the mass absorption coefficients calculated using GATE, XCOM, and Phy-X programs. According to the data obtained, the lowest value is 0.0571 g/cm^2, and the highest is 0.0810 g/cm^2. The mass absorption coefficient expresses the photon intensity remaining from the interaction of the incident radiation with the matter. According to these results, the highest radiation absorption property belongs to compound **2c** and is 0.0810 g/cm^2. This value was obtained at an energy value of 662 keV. As the energy increases, the μ_m value drops to 0.0802 g/cm^2 according to the Phy-X data. It reflects the interactions of carbon, nitrogen, oxygen, and hydrogen atoms in molecule **2c** with gamma rays. Each type of atom can contribute to different interaction mechanisms and determine the overall absorption properties of the compound. In particular, in such organic compounds, hydrogen atoms increase the neutron absorption capacity, while carbon and nitrogen atoms may be more effective in gamma-ray absorption processes. Compton scattering is the most common type of interaction with carbon and nitrogen atoms because photons with an energy of 662 keV are suitable for this process. The photoelectric effect is less common for nitrogen and carbon atoms at an energy of 662 keV, as this effect is generally more pronounced for photons with a lower energy. In the photoelectric effect, the energy must be below 511 keV, which is the rest mass energy of the electron. As the energy increases, interaction with matter and matter atoms will occur through Compton scattering or pair formation. The fact that the mass absorption coefficients are higher at 662 keV (Figs. 2a, 3a, 4a) indicates this situation. With an increase of energy, the mass absorption coefficient decreases for all materials. As seen in Figs. 2b, 3b, and 4b, the linear absorption coefficient, which expresses the path of gamma rays in the material, is higher at 662 keV and it decreases as the energy increases. The highest LAC value was obtained by GATE simulation and is 0.08636 cm^{-1}, and the lowest value is 0.05694 cm^{-1} at 1332 keV. Although there are no major differences between compounds **2a**–**2c**, the LAC and MAC values of **2c** are higher than the others. It is seen that increasing the number of C atoms increases radiation absorption. When we look at the HVL values, i.e., the

Table 4. Molecular weights and densities of compounds **2a**–**2c**

Compound no.	Formula	Molecular weight	Density, g/cm^3
2a	$C_{17}H_{23}N_3O$	285.4	1.001
2b	$C_{18}H_{25}N_3O$	299.4	0.946
2c	$C_{19}H_{27}N_3O$	313.4	0.887

Table 5. Mass absorption coefficients (MAC) of compounds **2a**–**2c** according to photon energies

Compound no.	μ_m (MAC), g/cm^2								
	662 keV			1173 keV			1332 keV		
	Phy-X	GATE	XCOM	Phy-X	GATE	XCOM	Phy-X	GATE	XCOM
2a	0.0798	0.0610	0.0568	0.0800	0.0608	0.0571	0.0800	0.0609	0.0571
2b	0.0807	0.0610	0.0572	0.0801	0.0612	0.0571	0.0801	0.0611	0.0572
2c	0.0810	0.0622	0.0575	0.0805	0.0613	0.0571	0.0802	0.0612	0.0573

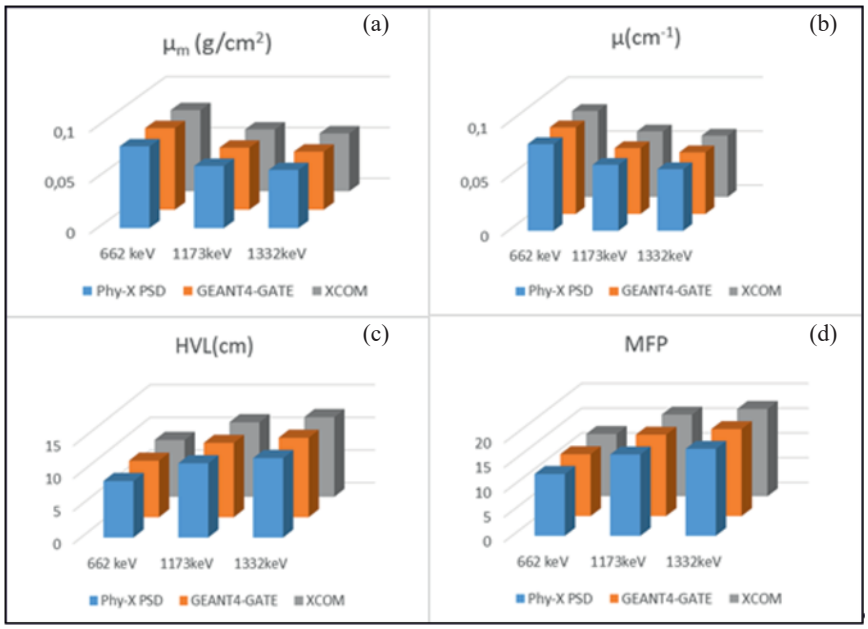


Fig. 2. Calculated (a) mass absorption coefficient (μ_m, g/cm^2), (b) linear absorption coefficient (μ), (c) half value thickness (HVL), and (d) mean free path (MFP) for compound **2a**.

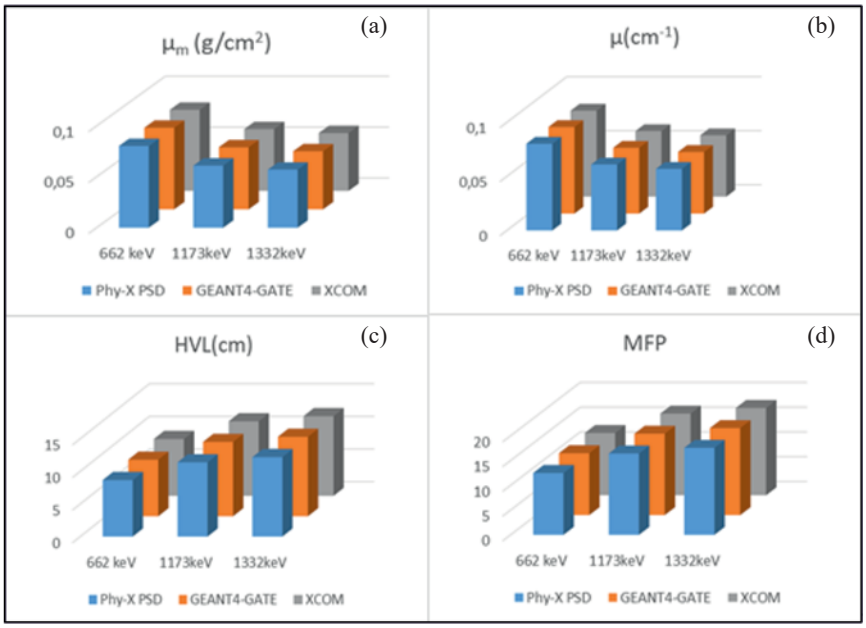


Fig. 3. Calculated (a) mass absorption coefficient (μ_m, g/cm^2), (b) linear absorption coefficient (μ), (c) half value thickness (HVL), and (d) mean free path (MFP) for compound **2b**.

thickness required to halve the initial amount of gamma rays in the transmitted energy (Figs. 2c, 3c, 4c), the highest value is 12.17 cm for compound **2a**, and this value increases in direct proportion to the energy. At 662 keV, this value decreases to 8.64 cm. The MFP value increases from 10.9506 cm to 17.62324 cm. These values were obtained as the energy increased from 662 to 1332 keV. The lowest MFP value (10.991 cm) is observed for compound **2c**. This value is expected to increase to 15.561 cm with increase in energy. The study shows that increasing the number of carbon atoms increases the capacity of compounds to absorb gamma rays. High carbon content provides a more effective radiation shielding feature. As the energy of gamma rays increases, HVL and MFP values also increase. This reveals that absorption of high-

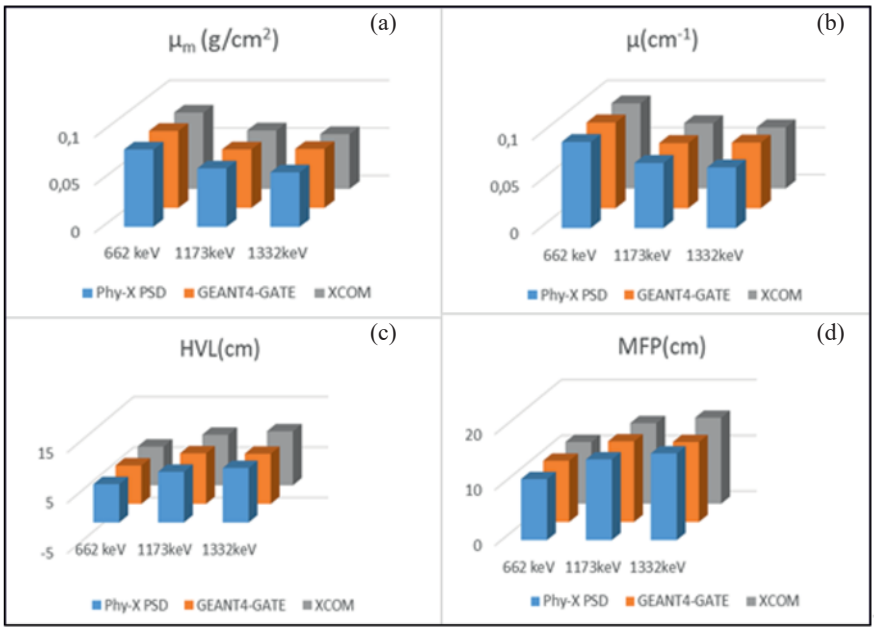


Fig. 4. Calculated (a) mass absorption coefficient (μ_m, g/cm^2), (b) linear absorption coefficient (μ), (c) half value thickness (HVL), and (d) mean free path (MFP) for compound **2c**.

energy gamma rays is more difficult and requires a thicker material. Compound **2c** stands out as a more effective gamma ray absorber at low energies, but this efficiency decreases as the energy level increases.

These findings show that the number of carbon atoms plays a critical role in the absorption of gamma rays and that the energy level significantly affects the absorption efficiency. Such studies can be an important guide in the design and optimization of radiation shielding materials. In particular, it offers valuable information on the selection and use of compounds to ensure safety standards in various applications. There are a limited number of studies with such materials in the literature. Jahan et al. [42] stated that polymers with high carbon content effectively absorb gamma rays. Naikvadi et al. [43] showed that the HVL and MFP values of different polymer composites vary depending on the energy level and that these values increase as the energy increases. Al-Ghamdi et al. [44] examined the absorption capacities of different organic compounds against gamma rays and stated that compounds with high carbon and oxygen content were more effective. Alsaab et al. [45] showed that the HVL and MFP values of different polymers and composite materials vary depending on the energy and that materials with high carbon content have especially lower HVL values. In the current study, we found that the HVL and MFP values of **2a** increased as the energy increased and that the carbon content increased the absorption capacity. These results are consistent with the literature findings and highlight the importance of energy-dependent HVL and MFP values of polymers.

Antimicrobial activity. The synthesized compounds were tested for their antimicrobial properties against a variety of microorganisms in vitro. The test panel included four Gram-positive bacteria (*Bacillus cereus*, *Bacillus subtilis*, *Staphylococcus aureus*, *Enterococcus faecalis*), four Gram-negative bacteria (*Escherichia coli*, *Yersinia pseudotuberculosis*, *Pseudomonas aeruginosa*, *Klebsiella pneumoniae*), and a yeast-like fungus (*Candida albicans*). Table 6 provides a summary of the findings, showing the minimum inhibitory concentrations (MIC) of the newly synthesized compounds in comparison to the MIC values of standard antibiotics used against the same microorganisms.

The antimicrobial activity of **2a**–**2c** revealed a consistent pattern of moderate inhibitory effects across a wide range of microorganisms. For most bacterial strains, the compounds exhibited MIC values of 312 μg/mL, indicating moderate but consistent antimicrobial activity. This was observed against Gram-positive strains such as *B. cereus*, *B. subtilis*, and *S. aureus*, as well as Gram-negative strains such as *E. coli* and *Y. pseudotuberculosis*. However, their activity was lower compared to the standard antibiotics, which generally had significantly lower MIC values. All compounds **2a**–**2c** exhibited weaker activity against

Table 6. Minimum inhibitory concentrations (μg/mL) of compounds **2a**–**2c** and reference antibiotics against tested microorganisms

Microorganism	**2a**	**2b**	**2c**	Ampicillin	Fluconazole
B. cereus	312	312	312	15	–
B. subtilis	312	312	312	10	–
Y. pseudotuberculosis	312	312	312	18	–
K. pneumoniae	625	625	625	16	–
E. coli	312	312	312	8	–
P. aeruginosa	625	625	625	128	–
S. aureus	312	312	312	10	–
E. faecalis	78	156	312	10	–
C. albicans	78	78	78	–	8

P. aeruginosa and *K. pneumoniae*, with MIC values of 625 μg/mL. This reduced efficacy is consistent with the known challenges in treating Gram-negative pathogens due to the protective outer membrane. In comparison, the standard antibiotic had MIC values of 128 and 16 μg/mL for *P. aeruginosa* and *K. pneumoniae*, respectively, highlighting the limitations of the synthesized compounds against these strains.

The three compounds showed varying levels of activity against *E. faecalis*. Compound **2a** demonstrated the highest potency with an MIC of 78 μg/mL, followed by compounds **2b** at 156 μg/mL and **2c** at 312 μg/mL. This suggests that compound **2a** may have greater efficacy against Gram-positive bacteria compared to the other two compounds. Interestingly, all three compounds showed strong antifungal activity against *C. albicans*, with MIC values of 78 μg/mL. This is notable, as the standard antibiotic showed only slightly better activity with an MIC of 8 μg/mL. This result highlights the potential of the synthesized compounds, particularly as antifungal agents.

Overall, the synthesized compounds demonstrated moderate, broad-spectrum antimicrobial activity, particularly against Gram-positive bacteria and *C. albicans*. While their activity against Gram-negative bacteria, especially *P. aeruginosa* and *K. pneumoniae*, was limited, their strong antifungal potential suggests that they may be promising candidates for further development, especially in the context of fungal infections. Compound **2a** stands out for its higher activity against *E. faecalis*, making it a potential lead compound for optimization. These results suggest that compound **2a** has promising antimicrobial potential against Gram-positive bacteria and fungal species.

Molecular docking study. Molecular docking studies were conducted to assess the binding affinity and interactions of compound **2a** with four target enzymes, all of which play crucial roles in bacterial metabolism and survival. The binding energies, inhibition constants (K_i), hydrogen bonds, and interacting amino acid residues are summarized in Table 7. The binding poses and interactions of compound **2a** with each receptor protein are illustrated in Fig. 5. In line with previous research emphasizing the targeting of vital bacterial pathways [46–49], key enzymes involved in essential cellular processes were selected for this study. These enzymes serve as critical targets for the disruption of bacterial metabolic and replication processes.

Compound **2a** exhibited a binding energy of –6.39 kcal/mol with beta-ketoacyl-ACP synthase III (PDB ID: 1HNJ) and a K_i value of 20.61 μM. The ligand formed four hydrogen bonds, with the most significant interaction occurring at Asn247, featuring a bond length of 1.94 Å. In addition to the hydrogen bonds, van der Waals interactions with Trp32, Arg36, and Phe213 contributed to the stability of the ligand–receptor complex. The ligand interaction profile included one conventional hydrogen bond, two carbon–hydrogen bonds, three π–σ bonds, two π–alkyl bonds, and one π–π T-shaped bond. Beta-ketoacyl-ACP synthase III is the key enzyme in bacterial fatty acid synthesis, and the strong interactions observed suggest that compound **2a** may act as an effective inhibitor of this pathway, thus disrupting cell wall formation and contributing to antibacterial activity [9, 50].

Docking analysis with glucosamine-6-phosphate synthase (PDB ID: 2VF5) resulted in a binding energy

Table 7. Binding energies, inhibition constants K_i, H-bond numbers, and interacted amino acid residues according to molecular docking study of compound **2a** with receptor proteins

Protein PDB ID	Binding energy, kcal/mol	K_i, μM	H-bond number	Van der Waals interactions	Interacting key residues
1HNJ	–6.39	20.61	4	Trp32, Arg36, Thr37, Ile156, Met207, Val212, Phe213, Asn274, Ala303, Gly305	Ala216, Leu220, His244, Ala246, Asn247, Ile250, Phe304
2VF5	–5.63	74.24	4	Cys300, Gly301, Ser303, Leu346, Gln348, Thr352, Thr355, Ser401, Leu484, Glu488, Lys603, Val605	Ala299, Thr302, Ser347, Ser349, Leu601, Ala602
5CDN	–5.52	90.57	3	Ala89, Val91, Ser98, Ser112, Met113, Gly115, Gly117, Thr220, Ile264, Pro265, Phe266, Gln267, Asn269	Glu88, Arg92, Gln95, Phe97, Val268
5MMN	–5.61	77.73	1	Asn46, Glu50, Arg76, Gln72, Gly77, Thr165, Met166	Val43, Ala47, Val71, Asp73, Ile78, Pro79 Arg136, Val167

of –5.63 kcal/mol and a K_i value of 74.24 μM. The ligand formed four hydrogen bonds, with the most significant occurring with Thr302 at 1.85 Å). The observed van der Waals interactions with Cys300, Gly301, and Leu484 also stabilized the ligand–receptor complex. The interaction profile included two conventional hydrogen bonds, two carbon–hydrogen bonds, three π–σ bonds, two π–alkyl bonds, and one alkyl bond. Although the binding energy was lower compared to beta-ketoacyl-ACP synthase III, the stable interactions suggest that compound **2a** could still exhibit antibacterial effects by targeting glucosamine-6-phosphate synthase, the key enzyme in the biosynthesis of bacterial cell walls. For DNA gyrase subunit A (PDB ID: 5CDN), compound **2a** exhibited a binding energy of –5.52 kcal/mol and a K_i value of 90.57 μM, indicating weaker binding affinity compared to the previous enzymes. The ligand formed three hydrogen bonds, with the most significant interaction occurring at Gln95 with a bond length of 3.19 Å. Other interactions included van der Waals contacts with the amino acid residues Ala89, Val91, and Ser112. The ligand interaction profile consisted of one conventional hydrogen bond, two carbon–hydrogen bonds, one π–σ bond, two π–anion bonds, and one π–π T-shaped bond. DNA gyrase A is a crucial enzyme for bacterial DNA replication, facilitating the introduction of negative supercoils into DNA in an ATP-dependent manner [51]. Although the binding affinity was lower, the ability of compound **2a** to interact with this enzyme suggests potential antibacterial activity, though less potent compared to the other targets. The docking results with *E. coli* DNA gyrase (GyrB; PDB ID: 5MMN) revealed a binding energy of –5.61 kcal/mol and a K_i value of 77.73 μM. The ligand formed one hydrogen bond with Asp73, a conserved residue within the ATP-binding site that plays a crucial role in the supercoiling activity of DNA gyrase [51]. Additional van der Waals interactions with Trp32, Ile156, and Ala303 residues contributed to the stabilization of the ligand within the active site. The binding profile of compound-**2a** with GyrB included one carbon–hydrogen bond, two π–alkyl bonds, four alkyl bonds, one π–cation bond, and one π-donor bond. The strong interaction with Asp73 (bond length 2.92 Å) suggests that compound **2a** could inhibit bacterial DNA replication, offering significant antibacterial potential against *E. coli*.

Overall, compound **2a** showed the strongest binding affinity with beta-ketoacyl-ACP synthase III, as evidenced by the lowest binding energy and K_i value. This suggests that compound **2a** may serve as a potent inhibitor of bacterial fatty acid biosynthesis, a key target in the development of antibacterial agents. The interactions observed with glucosamine-6-phosphate synthase and DNA gyrases A and B indicate that compound **2a** has a broad range of potential antibacterial effects. Notably, its ability to interact with Asp73 in *E. coli* DNA gyrase highlights its potential as a promising antibacterial agent targeting DNA replication in bacteria [51]. Molecular docking, as employed in this study, provides a powerful method for predicting the binding interactions of small molecules with target proteins. This approach significantly reduces the time and cost associated with experimental trial-and-error

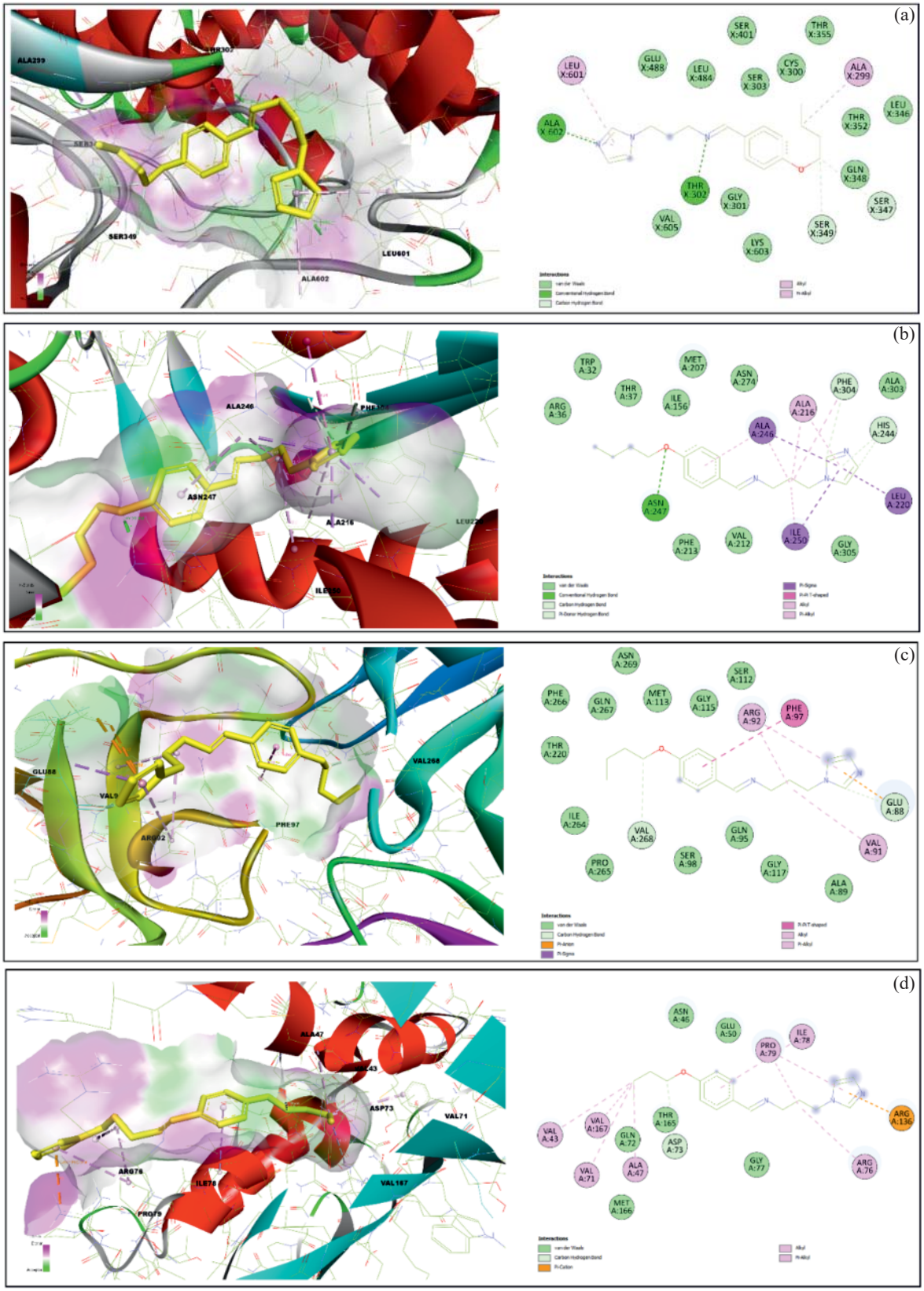


Fig. 5. 2D and 3D representations of the docked poses of compound **2a** with essential residues in the active sites of (a) glucosamine-6-phosphate synthase (PDB ID: 2VF5), (b) beta-ketoacyl-ACP synthase III (PDB ID: 1HNJ), (c) *S.aureus* DNA gyrase (PDB ID: 5CDN), and (d) *E. coli* DNA gyrase B 24 kDa ATPase domain (PDB ID: 5MMN).

methods, allowing for the identification of new antibacterial agents based on first principles [9, 50]. The docking results of compound **2a** align with its predicted biological activity, supporting its potential as a novel antibacterial compound with the ability to inhibit key bacterial enzymes.

EXPERIMENTAL

The IR spectra were recorded in KBr on a Perkin Elmer 1600 FT-IR spectrometer in the range of 4000–400 cm^{-1}. The ^1H and ^{13}C NMR spectra were taken on a Bruker spectrometer operating at 400 and 100 MHz, respectively, using DMSO-d_6 as solvent. The solvents and chemicals used in the synthesis and structure elucidation were obtained from Fluka, Merck, and Aldrich, and all solvents were subjected to appropriate purification and drying procedures.

Compounds 2a–2c (*general procedure***).** A mixture of 4-(alkoxy))benzaldehyde derivative **1a**–**1c** (prepared according to [52]), 3-(1*H*-imidazol-1-yl)propan-1-amine, and 50 mL of ethyl alcohol was heated with stirring for 5–6 h. The progress of the reaction was monitored by thin layer chromatography (TLC). After completion of the reaction, the mixture was cooled and evaporated, and the oily residue was purified by recrystallization from ethanol–water (3:1).

(*E*)-1-(4-Butoxyphenyl)-*N*-[3-(1*H*-imidazol-1-yl)-propyl]methanimine (2a). Yield 84.70%. IR spectrum, ν, cm^{-1}: 2933 (C–H), 1643 (C=N), 1604 (C=C), 1243 (C–O–C). ^1H NMR spectrum, δ, ppm: 0.92 t (3H, CH_3), 1.38–1.47 m (2H, CH_2), 1.66–1.73 m (2H, CH_2), 3.97–4.06 m (2H, OCH_2), 2.00–2.07 m (2H, CH_2), 3.46 t (2H, CH_2), 3.97–4.06 m (2H, CH_2), 7.65–7.69 m (4H, H_{arom}), 6.91 d and 6.98 d (1H each, 4-H, 5-H), 7.20 s (1H, 2-H), 8.22 s (1H, N=CH). ^{13}C NMR, δ_C, ppm: 14.13 (CH_3), 19.18 (CH_2), 31.13 (CH_2), 67.76 (OCH_2), 32.42 (CH_2), 44.53 (CH_2), 57.62 (CH_2), 114.70 (2C, CH), 129.16 (2C), 129.99 (2C, CH), 161.12 (2C)], 119.65 (CH), 128.75 (CH), 137.72 (CH), 161.15 (N=CH).

(*E*)-*N*-(3-(1*H*-Imidazol-1-yl)propyl)-1-(4-(pentyl-oxy)phenyl)methanimine (2b). Yield 88.85%. IR spectrum, ν, cm^{-1}: 2933 (C–H), 1642 (C=N), 1604 (C=C), 1245 (C–O–C). ^1H NMR spectrum, δ, ppm: 0.89 t (3H, CH_3), 1.28–1.42 m (4H, CH_2), 1.67–1.73 m (2H, CH_2), 3.97–4.06 m (2H, OCH_2), 2.00–2.07 m (2H, CH_2), 3.46 t (2H, CH_2), 3.97–4.06 m (2H, CH_2), 7.64–7.69 m (4H, H_{arom}), 6.91 d and 6.98 d (1H each, 4-H, 5-H), 7.20 s (1H, 2-H), 8.23 s (1H, N=CH). ^{13}C NMR spectrum, δ_C: 14.36 (CH_3), 22.36 (CH_2), 28.02 (CH_2), 28.63 (CH_2), 68.04 (OCH_2), 32.42 (CH_2), 44.52 (CH_2), 57.63 (CH_2), 114.90 (2C, CH), 129.17 (2C), 129.98 (2C, CH), 161.10 (2C), 119.66 (CH), 128.67 (CH), 137.63 (CH), 161.15 (N=CH).

(*E*)-1-[4-(Hexyloxy)phenyl]-*N*-[3-(1*H*-imidazol-1-yl)propyl]methanimine (2c). Yield 85.65%. IR spectrum, ν, cm^{-1}: 2930 (C–H), 1642 (C=N), 1604 (C=C), 1244 (C–O–C). ^1H NMR spectrum, δ, ppm: 0.86 t (3H, CH_3), 1.28–1.30 m (2H, CH_2), 1.36–1.41 m (2H, CH_2), 1.66–1.73 m (2H, CH_2), 3.96–4.04 m (2H, OCH_2), 2.00–2.07 m (2H, CH_2), 3.45 t (2H, CH_2), 3.96–4.04 m (2H, CH_2), 7.64–7.69 m (4H, H_{arom}), 6.91 d and 6.97 d (1H each, 4-H, 5-H), 7.19 s (1H, 2-H), 8.22 s (1H, N=CH). ^{13}C NMR spectrum, δ_C, ppm, δ_C, ppm: 14.35 (CH_3), 22.55 (CH_2), 25.63 (CH_2), 29.05 (CH_2), 31.47 (CH_2), 68.05 (OCH_2), 32.35 (CH_2), 44.52 (CH_2), 57.63 (CH_2), 114.71 (2C, CH), 129.08 (2C), 129.98 (2C, CH), 161.10 (2C)], 119.56 (CH), 128.75 (CH), 137.72 (CH), 161.22 (N=CH).

Computational details. Gaussian 09 [53] software package was used for quantum chemical calculations of compounds **2a–2c**. The optimization of the molecules was performed by choosing DFT/B3LYP method and 6-311++G(*d*,*p*) [54, 55] basis set. GausView [56] program was used for visualization of the optimized structures. The vibrational frequencies were calculated at the same level of theory. For the calculated vibrational frequencies of these three molecules, scale factors of 0.983 and 0.958 were used above and below 1700 cm^{-1} [57, 58]. Chemical shifts were calculated using the GIAO [59, 60] approach. ^1H and ^{13}C chemical shift calculations were performed using scale factors of 31.9681 and 184.0184 ppm [61].

Theoretical information for gamma-ray absorption. For the measurement process, the experimental setup shown in Fig. 6 was established, a NaI detector was designed, and the material was placed in front of the gamma source to minimize the scattered light depending on the sample area [62]. The linear attenuation coefficient (LAC) of the samples was examined using the Beer–Lambert law given in Eq. (1). The LAC values were calculated by substituting the MAC values obtained from the simulations according to the mass attenuation coefficient (MAC) calculated by Eq. (2). Additionally, other relevant parameters such as HVL (half value thickness) and MFP (mean free path) were obtained using Eqs. (3) and (4), respectively.

$$\mu\,(\mathrm{LAC}) = \frac{1}{x}\ln\left(\frac{I_0}{I}\right), \qquad (1)$$

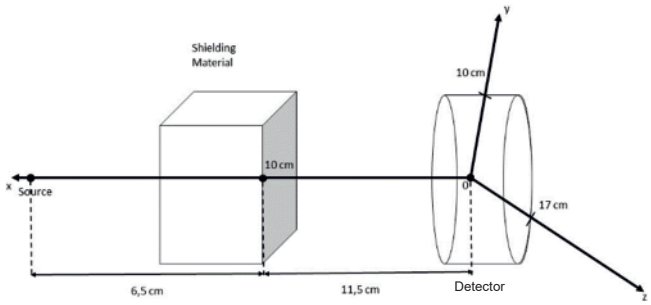


Fig. 6. Gate simulation setup.

$$\mu_m\,(\mathrm{MAC}) = \frac{\mu\,(\mathrm{LAC})}{\rho}, \quad (2)$$

$$\mathrm{HVL} = \frac{\ln(2)}{\mu}, \quad (3)$$

$$\mathrm{MFP} = \frac{1}{\mu}. \quad (4)$$

In Eq. (1), μ (LAC) is the linear attenuation coefficient; x represents the thickness of the material, I represents the intensity of gamma rays reaching the detector after interacting with the material, and I_0 represents the intensity of gamma rays reaching the detector without interacting with the material [63]. In Eq. (2), the mass attenuation coefficient μ_m (MAC) shows the spread of radiation after its interaction with atoms of the material, and ρ is the density of the material [64]. HVL refers to the thickness required to halve the intensity of incoming radiation. MFP is the average thickness through which radiation can travel without interacting with matter atoms. These values are inversely proportional to the linear absorption coefficient, and as the absorption of radiation increases, HVL and MFP values decrease.

Three different theoretical methods were used to simulate gamma-ray absorption features: XCOM [65], Phy-X/PSD [66], and GATE (Geant4 Application for Tomographic Emission).

The detailed procedures for antimicrobial assay and molecular docking study are given in Supplementary Materials.

CONCLUSIONS

Imidazole Schiff bases **2a**–**2c** were synthesized, and their structure was confirmed by FTIR and NMR spectroscopic methods. Their molecular structures were optimized by DFT calculations at the B3LYP/6-311++G(*d*,*p*) level of theory. The IR and NMR spectral parameters of compounds **2a**–**2c** were calculated and compared with the experimental data. The radiation shielding properties and antimicrobial activities of compounds **2a**–**2c** depending on the carbon content in the hydrocarbon chain were investigated. Gamma ray shielding parameters of these compounds were examined with Monte Carlo-based Geant4-GATE, Phy-X/PSD, and XCOM simulations. The higher mass absorption coefficient (MAC) was found for compound **2c** with a higher number of carbon atoms. Its value is 0.0669 g/cm^2 on average in all three simulations at 662 keV, and it decreases to 0.0662 g/cm^2 with increasing energy. Compound **2a** stands out for its higher activity against *E. faecalis*, making it a potential lead compound for optimization. The docking results for compound **2a** align with its predicted biological activity, supporting its potential as a novel antibacterial compound with the ability to inhibit key bacterial enzymes.

ACKNOWLEDGMENTS

The numerical calculations reported in this paper were fully performed at TUBITAK ULAKBIM, High Performance and Grid Computing Center (TRUBA resources).

FUNDING

This work was supported by ongoing institutional funding. No additional grants to carry out or direct this particular research were obtained.

CONFLICT OF INTEREST

The authors declare that they have no conflicts of interest.

SUPPLEMENTARY INFORMATION

The online version contains supplementary material available at https://doi.org/10.1134/S1070428025601293.

REFERENCES

1. Tanak, H., Köysal, Y., Ünver, Y., Yavuz, M., Işık, Ş., and Sancak, K., *Struct. Chem*., 2009, vol. 20, p. 409. https://doi.org/10.1007/s11224-009-9425-0
2. Rani, N., Sharma, A., and Singh, R., *Mini-Rev. Med. Chem*., 2013, vol. 13, p. 1812. https://doi.org/10.2174/13895575113136660091
3. Sancak, K., Ünver, Y., Tanak, H., Değirmencioğlu, İ., Düğdü, E., Er, M., and Işık, Ş., *J. Inclusion Phenom. Macrocycl. Chem*., 2010, vol. 67, p. 325. https://doi.org/10.1007/s10847-009-9714-7
4. Graβmann, S., Sadek, B., Ligneau, X., Selz, S., Ganellin, C.R., Arrang, J.M., Schwartz, J.C., Stark, H., and Schunack, W., *Eur. J. Pharm. Sci*., 2002, vol. 15, p. 367. https://doi.org/10.1016/S0928-0987(02)00024-6
5. Jain, R., Vangapandu, S., Jain, M., Kaur, N., Singh, S., and Singh, P.P., *Bioorg. Med. Chem. Lett*., 2002, vol. 12, p. 1700. https://doi.org/10.1016/S0960-894X(02)00289-5
6. Soujanya, Y. and Sastry, G.N., *Tetrahedron Lett*., 2007, vol. 48, p. 2109. https://doi.org/10.1016/j.tetlet.2007.01.131
7. Hussain, T., Siddiqui, H.L., Zia-ur-Rehman, M., Yasinzai, M.M., and Parvez, M., *Eur. J. Med. Chem*., 2009, vol. 44, p. 4654. https://doi.org/10.1016/j.ejmech.2009.06.038
8. Nguyen, D.N., Stump, C.A., Walsh, E.S., Fernandes, C., Davide, J.P., Ellis-Hutchings, M., Robinson, R.G., Williams, T.M., Lobell, R.B., Huber, H.E., and Buser, C.A., *Bioorg. Med. Chem. Lett*., 2002, vol. 12, p. 1269. https://doi.org/10.1016/S0960-894X(02)00154-3
9. Chen, J., Wang, Z., Lu, Y., Dalton, J.T., Miller, D.D., and Li, W., *Bioorg. Med. Chem. Lett*., 2008, vol. 18, p. 3183. https://doi.org/10.1016/j.bmcl.2008.04.073
10. Dominianni, S.J. and Yen, T.T., *J. Med. Chem*., 1989, vol. 32, p. 2301. https://doi.org/10.1021/jm00130a013
11. Tweit, R.C., Kreider, E.M., and Muir, A.D., *J. Med. Chem*., 1973, vol. 16, p. 1161. https://doi.org/10.1021/jm00268a021
12. Davidson, G.S., *Int. J. Pharm. Compd*., 2006, vol. 10, p. 434.
13. Klásek, A., Lyčka, A., and Halčapek, M., *Tetrahedron*, 2007, vol. 63, p. 7059. https://doi.org/10.1016/j.tet.2007.05.012
14. Verma, A., Joshi, S., and Singh, D., *J. Chem*., 2013, vol. 2013, article ID: 329412. https://doi.org/10.1155/2013/329412
15. Ünver, Y., Sancak, K., Çelik, F., Birinci, E., Küçük, M., Soylu, S., and Burnaz, N.A., *Eur. J. Med. Chem*., 2014, vol. 84, p. 639. https://doi.org/10.1016/j.ejmech.2014.01.014
16. Sharaby, C.M., Amine, M.F., and Hamed, A.A., *J. Mol. Struct*., 2017, vol. 1134, p. 208. https://doi.org/10.1016/j.molstruc.2016.12.070
17. Süleymanoğlu, N., Demir, E., Direkel, Ş., and Ünver, Y., *J. Mol. Struct*., 2020, vol. 1218, article ID: 128522. https://doi.org/10.1016/j.molstruc.2020.128522
18. Ünver, Y., Deniz, S., Çelik, F., Akar, Z., Küçük, M., and Sancak, K., *J. Enzyme Inhib. Med. Chem*., 2016, vol. 31, p. 89. https://doi.org/10.1080/14756366.2016.1206088
19. Süleymanoğlu, N., Çelik, F., Ustabaş, R., Güler, H.İ., Şahin, H., Direkel, Ş., and Ünver, Y., *Russ. J. Phys. Chem. A*, 2023, vol. 97, p. 3037. https://doi.org/10.1134/S0036024423130162
20. Süleymanoğlu, N., Ustabaş, R., Ünver, Y., Alpaslan, Y.B., Direkel, Ş., and Karaman, Ü., *J. Mol. Struct*., 2019, vol. 1182, p. 36. https://doi.org/10.1016/j.molstruc.2019.01.005
21. Ünver, Y., Tuluk, M., Kahriman, N., Emirik, M., Bektaş, E., and Direkel, Ş., *Russ. J. Gen. Chem*., 2019, vol. 89, p. 794. https://doi.org/10.1134/S107036321904025X
22. Seçkin, T., Köytepe, S., Demir, S., Özdemir, İ., and Çetinkaya, B., *J. Inorg. Organomet. Polym*., 2003, vol. 13, p. 223. https://doi.org/10.1023/A:1026144010812
23. Ashraf, M., Wajid, A., Mahmood, K., Maah, M., and Yusoff, I., *Orient. J. Chem*., 2011, vol. 27, p. 363.
24. Ozaslan, M., Karagöz, I.D., Kılıç, I.H., and Güldür, M.E., *Afr. J. Biotechnol*., 2011, vol. 10, p. 2375.
25. Golcu, A., Tümer, M., Demirelli, H., and Wheatley, R., *Inorg. Chim. Acta*, 2005, vol. 358, p. 1785. https://doi.org/10.1016/j.ica.2004.11.026
26. da Silva, C., da Silva, D., Modolo, L., Alves, R., de Resende, M.A., Martins, C.V.B., and de Fátima, Â., *J. Adv. Res*., 2011, vol. 2, p. 1. https://doi.org/10.1016/j.jare.2010.05.004
27. Rehman, W., Baloch, M.K., Muhammad, B., Badshah, A., and Khan, K.M., *Chin. Sci. Bull*., 2004, vol. 49, p. 119. https://doi.org/10.1360/03wb0174
28. Emregül, K.C., Düzgün, E., and Atakol, O., *Corros. Sci*., 2006, vol. 50, p. 3243. https://doi.org/10.1016/j.corsci.2005.11.016
29. Wang, C., Smith, J., Anderson, R., Thompson, S., and Johnson, C., *Prog. Nucl. Energy*, 2021, vol. 137, article ID: 103964.
30. Wood, J., *International Atomic Energy Agency*: Pergamon Turkey, 1982, p. 192.
31. Akçaalan, U., *Afyon Kocatepe Üniversitesi Fen Bilimleri Enstitüsü*, Afyon, 2015.
32. Singh, V.P., Badiger, N.M., and Kaewkhao, J., *J. Non-Cryst. Solids*, 2014, vol. 404, p. 167. https://doi.org/10.1016/J.JNONCRYSOL.2014.08.003

33. Wu, Y., Zhang, Q.-P., Zhou, D., Zhou, Y.-L., and Zheng, J., *J. Alloys Compd*., 2017, vol. 727, p. 1027. https://doi.org/10.1016/j.jallcom.2017.08.219
34. Abou Hussein, E.M., Madbouly, A.M., and El Alaily, N.A., *J. Non-Cryst. Solids*, 2021, vol. 570, article ID: 121021. https://doi.org/10.1016/j.jnoncrysol.2021.121021
35. Muteeb, G., Rehman, M.T., Shahwan, M., and Aatif, M., *Pharmaceuticals*, 2023, vol. 16, no. 11, article no. 1615. https://doi.org/10.3390/ph16111615
36. Sebbar, N.K., Ellouz, M., Ouzidan, Y., Kaur, M., Essassi, E.M., and Jasinski, J.P., *IUCrData*, 2017, vol. 2, no. 6, article ID: 170890. https://doi.org/10.1107/S2414314617008902
37. Bugenhagen, B., Al Jasem, Y., and Thiemann, T., *Acta Crystallogr., Sect. E*, 2014, vol. 70, no. 10, p. 231. https://doi.org/10.1107/S1600536814020571
38. Abbas, A., Khawar Rauf, M., Bolte, M., and Hasan, A., *Acta Crystallogr., Sect. E*, 2009, vol. 65, p. o1281. https://doi.org/10.1107/S1600536809017358
39. Dudeja, N., Arreaga, B.C., Brannon, J.P., and Stieber, S.C.E., *Acta Crystallogr., Sect. E*, 2023, vol. 79, no. 11, p. 1079. https://doi.org/10.1107/S2056989023009179
40. McClements, I.F.C., Wiesler, R., and Tanski, J.M., *Acta Crystallogr., Sect. E*, 2023, vol. 79, no. 7, p. 678. https://doi.org/10.1107/S2056989023005480
41. Cheng, H., *Acta Crystallogr., Sect. E*, 2013, vol. 69, p. o1721. https://doi.org/10.1107/S1600536813029024
42. Jahan, M.S., Hossain, S., Sayeed, M.A., Das, S.C., Grammatikos, S., Pingky, S.Y., and Khan, R.A., *Radiat. Eff. Defects Solids*, 2024, vol. 179, p. 1132. https://doi.org/10.1080/10420150.2024.2332195
43. Naikwadi, A.T., Sharma, B.K., Bhatt, K.D., and Mahanwar, P.A., *Front. Chem*., 2022, vol. 10, article ID: 837111. https://doi.org/10.3389/fchem.2022.837111
44. Al-Ghamdi, H., Elsafi, M., Almuqrin, A.H., Yasmin, S., and Sayyed, M.I., *Materials*, 2022, vol. 15, no. 15, p. 5310. https://doi.org/10.3390/ma15155310
45. Alsaab, A.H. and Zeghib, S., *J. Radiat. Res. Appl. Sci*., 2023, vol. 16, no. 4, article ID: 100708. https://doi.org/10.1016/j.jrras.2023.100708
46. Kaur, H., Gahlawat, S., Singh, J., and Narasimhan, B., *Curr. Drug Targets*, 2019, vol. 20, no. 15, p. 1587. https://doi.org/10.2174/1389450120666190618122359
47. Ünver, Y., Süleymanoğlu, N., Ustabaş, R., Bektaş, K.İ., Bektaş, E., and Güler, H.İ., *J. Biomol. Struct. Dyn*., 2022, vol. 40, p. 12990. https://doi.org/10.1080/07391102.2021.1977708
48. Çelik, F., Aydın, A., Bektaş, K.İ., Güler, H.İ., Nalça-oğlu, A., and Ünver, Y., *Russ. J. Gen. Chem*., 2022, vol. 92, p. 2145. https://doi.org/10.1134/S1070363222100279
49. Mohammed Musthafa, T.N., Snigdha, K., Asiri, A.M., Sobahi, T.R., and Asad, M., *J. Mol. Struct*., 2023, vol. 1271, article ID: 133993. https://doi.org/10.1016/j.molstruc.2022.133993
50. Raj, S., Sasidharan, S., Dubey, V.K., and Saudagar, P., *PLoS One*, 2019, vol. 14, article ID: e0221331. https://doi.org/10.1371/journal.pone.0221331
51. Panchaud, P., Bruyère, T., Blumstein, A.-C., Bur, D., Chambovey, A., Ertel, E.A., Gude, M., Hubschwerlen, C., Jacob, L., Kimmerlin, T., Pfeifer, T., Prade, L., Seiler, P., Ritz, D., and Rueedi, G., *J. Med. Chem*., 2017, vol. 60, p. 3755. https://doi.org/10.1021/acs.jmedchem.6b01772
52. Hasan, A., Abbas, A., and Akhtar, M.N., *Molecules*, 2011, vol. 16, p. 7789. https://doi.org/10.3390/molecules16097789
53. Frisch, M.J., Trucks, G.W., Schlegel, H.B., Scuseria, G.E., Robb, M.A., Cheeseman, J.R., Scalmani, G., Barone, V., Mennucci, B., Petersson, G.A., Nakatsuji, H., Caricato, M., Li, X., Hratchian, H.P., Izmaylov, A.F., Bloino, J., Zheng, G., Sonnenberg, J.L., Hada, M., Ehara, M., Toyota, K., Fukuda, R., Hasegawa, J., Ishida, M., Nakajima, T., Honda, Y., Kitao, O., Nakai, H., Vreven, T., Montgomery, J.A., Jr., Peralta, J.E., Ogliaro, F., Bearpark, M., Heyd, J.J., Brothers, E., Kudin, K.N., Staroverov, V.N., Kobayashi, R., Normand, J., Raghavachari, K., Rendell, A., Burant, J.C., Iyengar, S.S., Tomasi, J., Cossi, M., Rega, N., Millam, J.M., Klene, M., Knox, J.E., Cross, J.B., Bakken, V., Adamo, C., Jaramillo, J., Gomperts, R., Stratmann, R.E., Yazyev, O., Austin, A.J., Cammi, R., Pomelli, C., Ochterski, J.W., Martin, R.L., Morokuma, K., Zakrzewski, V.G., Voth, G.A., Salvador, P., Dannenberg, J.J., Dapprich, S., Daniels, A.D., Farkas, Ö., Foresman, J.B., Ortiz, J.V., Cioslowski, J., and Fox, D.J., *Gaussian 09, Revision A.1*, Wallingford CT: Gaussian, 2009.
54. Becke, A.D., *J. Chem. Phys*., 1993, vol. 98, p. 5648. https://doi.org/10.1063/1.464913
55. Lee, C., Yang, W., and Parr, R.G., *Phys. Rev. B*, 1988, vol. 37, p. 785. https://doi.org/10.1103/PhysRevB.37.785
56. Dennington, R.D., Keith, T.A., and Millam, J.M., GaussView, Version 5.0, Semichem Inc., Shawnee Mission, KS, 2009.
57. Abbas, A., Gökçe, H., Bahçeli, S., and Naseer, M.M., *J. Mol. Struct*., 2014, vol. 1075, p. 352. https://doi.org/10.1016/j.molstruc.2014.07.001
58. Gökçe, H., Öztürk, N., Taşan, M., Alpaslan, Y.B., and Alpaslan, G., *Spectrosc. Lett*., 2016, vol. 49, p. 167. https://doi.org/10.1080/00387010.2015.1114952

59. Ditchfield, R.J., *J. Chem. Phys*., 1972, vol. 56, p. 5688. https://doi.org/10.1063/1.1677088
60. Wolinski, K., Hinton, J.F., and Pulay, P., *J. Am. Chem. Soc*., 1990, vol. 112, p. 8251. https://doi.org/10.1021/ja00179a005
61. İskeleli, N.O., Alpaslan, Y.B., Direkel, Ş., Ertürk, G., Süleymanoğlu, N., and Ustabaş, R., *Spectrochim. Acta, Part A*, 2015, vol. 139, p. 356. https://doi.org/10.1016/j.saa.2014.12.071
62. Coşkun, A., Çetin, B., Yiğitoğlu, İ., and Topaklı, H., *Int. J. Comput. Exp. Sci. Eng*., 2023, vol. 9, p. 274. https://orcid.org/0000-0003-4771-1558
63. Lynch, W.G., *Phys. Today*, 1989. https://doi.org/10.1063/1.2810884
64. Kaewjang, S., Maghanemi, U., Kothan, S., Kim, H.J., Limkitjaroenporn, P., and Kaewkhao, J., *Nucl. Eng. Des*., 2014, vol. 280, p. 21. https://doi.org/10.1016/j.nucengdes.2014.08.030
65. Berger, M., and Hubbel, J.H., *XCOM: Photon Cross Sections on a Personal Computer*, Gaithersburg: National Institute of Standards and Technology, 1987.
66. Şakar, E., Özpolat, Ö.F., Alım, B., Sayyed, M.I., and Kurudirek, M., *Radiat. Phys. Chem*., 2020, vol. 166, article ID: 108496. https://doi.org/10.1016/j.radphyschem.2019.108496

Publisher's Note. Pleiades Publishing remains neutral with regard to jurisdictional claims in published maps and institutional affiliations.

AI tools may have been used in the translation or editing of the article.